Physics of Fluids

RESEARCH ARTICLE | AUGUST 16 2023

Study on the stall vortex and vibration characteristics in multi-stage pump under natural flow condition

Runze Zhou (周润泽) ; Houlin Liu (刘厚林) ; Liang Dong (董亮); Kim Tiow Ooi ; Cui Dai (代翠); Runan Hua (华如南)

Physics of Fluids 35, 084117 (2023)
https://doi.org/10.1063/5.0160366

Physics of Fluids ARTICLE pubs.aip.org/aip/pof

Study on the stall vortex and vibration characteristics in multi-stage pump under natural flow condition

Cite as: Phys. Fluids **35**, 084117 (2023); doi: 10.1063/5.0160366
Submitted: 1 June 2023 · Accepted: 27 July 2023 ·
Published Online: 16 August 2023

Runze Zhou (周润泽),[1,2] Houlin Liu (刘厚林),[2,3,a)] Liang Dong (董亮),[2,3] Kim Tiow Ooi,[1] Cui Dai (代翠),[4] and Runan Hua (华如南)[5]

AFFILIATIONS

[1]School of Mechanical and Aerospace Engineering, Nanyang Technological University, 50 Nanyang Avenue, 639798, Singapore
[2]National Research Center of Pumps, Jiangsu University, Zhenjiang 212013, China
[3]Research Center of Fluid Machinery Engineering and Technology, Jiangsu University, Zhenjiang 212013, China
[4]School of Energy and Power Engineering, Jiangsu University, Zhenjiang 212013, China
[5]Wuhan Second Ship Design and Research Institute, Wuhan, Hubei 430060, China

[a)]**Author to whom correspondence should be addressed:** liuhoulin@ujs.edu.cn

ABSTRACT

When a vessel reaches a specific speed, the circulating pump in the cooling system stops driving. It relies only on the kinetic energy its speed generates to provide cooling seawater for the condenser. This cooling strategy is known as natural flow cooling. Under natural flow conditions, the impeller rotates passively due to flow impact, and the circulating pump serves as a significant resistance component in the cooling system. The unstable flow within a pump is primarily attributed to the varying scales of stall vortex, which can induce vibration and potentially result in severe damage to components. To investigate the generation of stall vortex and vibration characteristics under natural flow conditions, the numerical simulation method was employed to study the structure and motion characteristics of stall vortex in multi-stage pumps at different flow rates. Moreover, vibration signals were collected through a natural flow experiment, and the obtained data were analyzed using empirical mode decomposition with singular value decomposition and wavelet transform methods. The result indicates that natural flow conditions can be categorized into impeller stuck and passive rotation. During passive rotation, the speed increases linearly with the flow rate. Thus, the blade inlet's attack angle remains consistent at different flow rates, making the internal flow features similar. The stretching and bending of the stall vortex structure primarily cause the variation of the vorticity. Additionally, the internal structure and motion pattern of stall vortex exhibit similarities. The excitation force increases continuously with the flow rate and is related to the effects of flow losses and turbulent kinetic energy. Vibration energy caused by stall vortex and rotor–stator interference is mainly concentrated in the low-frequency band.

I. INTRODUCTION

Modern high-speed vessels and nuclear-powered submarines commonly employ a natural flow cooling strategy. This approach utilizes the kinetic energy generated by vessel's own speed to provide cooling seawater to the condenser when the sailing speed meets the minimum requirements for natural flow cooling. Under natural flow conditions, the cooling system circulating pump is in the form of a non-driven resistance element. The natural flow exerts a torque on the rotor, enabling it to overcome mechanical resistance and passively rotate at a speed that varies with the inlet flow rate. This strategy effectively reduces energy consumption and vibration noise caused by the motor drive. However, the energy conversion mechanism in the circulating pump under natural flow conditions is significantly different from standard pump conditions, resulting in the generation of stall vortexes with different scales and numbers inside the pump. The unstable flow caused by stall vortexes during the development, shedding, and dissipation process, as well as the rotor–stator interference, excites the pump structure vibration, negatively impacting its operational reliability of the pump and shortening service life.[1,2] Moreover, the structural vibration of the pump generates noise, which compromises the acoustic stealth performance of the vessel.

Many scholars have conducted extensive research on the characteristics of stall vortex inside the flow field of rotating machinery. Sinha *et al.*[3] employed particle image velocimetry (PIV) and pressure pulsation measurements to investigate the onset and development of rotational stall in a centrifugal pump. Liu *et al.*[4] studied the transmission mechanism of rotating stall vortex inside the impeller using a refractive index matching experimental bench and high-frequency PIV system. They found that the stall vortex frequency is inversely proportional to the rotational speed and positively proportional to the flow rate. Feng *et al.*[5] identified that the prominent pressure pulsation between the two sides of the blades generates a stall vortex on the suction side of the inlet diffuser, and the stall cell rotates in the opposite direction to the impeller with $f_n/600$. Additionally, when the number of guide vanes is a multiple of the stall cell number, an alternate stall occurs, and the large-scale vortex in the flow channel appears to sway.[6] As the stall cells grow, they obstruct the flow channel, move toward the pressure side, and decay. Li *et al.*[7,8] accurately calculated the stall cells and circumferential propagation velocity under different conditions based on the pressure fluctuation characteristics, and proposed that the blocking effect of stall cells on flow channels would affect the flow structure in rim flow. Ji *et al.*[9] utilized entropy production analysis to investigate the distribution of high energy loss regions inside the pump and revealed that the tip clearance size significantly impacts the hydraulic loss in the stall region. Zhao *et al.*[10] studied the relationship between the unsteady spatiotemporal evolution of the stalled vortex structure and the kinetic energy conversion and found that the critical stall condition has a greater kinetic energy dissipation. Jia *et al.*[11–13] investigated the pressure pulsation characteristics caused by the tip leakage vortex (TLV) in the pump under unpowered drive conditions and proposed that the compression–expansion term determines the strength of the TLV core.

Unstable flow phenomena, such as stall vortex and backflow, can increase vibration in the pump sets. Regarding the research on pump vibration, Luo *et al.*[14] proposed that the abnormal vibration frequencies caused by backflow and rotational stall are mainly concentrated in the low-frequency band, approximately 0.23–0.25 times the rotational frequency. Bai *et al.*[15] established that flow rate significantly affects pump inlet and outlet vibration, with main vibration frequencies ranging from one to four times the blade passing frequency (BPF). Khalifa *et al.*[16] found a strong correlation between vibration and the pressure pulsation behavior of the pump, particularly at high speeds and off-design flow rates, which excite stronger vibrations. Furthermore, Wang *et al.*[17] presented that rotor–stator interaction (RSI) induces strong unsteady flow and pressure pulsation in the pump, causing severe vibration. Pu *et al.*[18] developed a method to analyze vibration utilizing the Euler head density function (EHDF) by quantifying the vorticity and local Euler head, which can predict the structural location of the low-speed vortex and vibration level. Cui *et al.*[19] found that the interaction between the tail vortex core and the volute produces significant pressure pulsation and radial force, tightly related to the pump shaft vibration. The impeller's complex vortex, consisting of tip leakage vortex (TLV), reverse flow vortex, passage vortex, and tip separation vortex, causes unstable flow inside the pump. Wang *et al.*[20] analyzed the vibration characteristic frequency with high amplitude caused by unsteady flow based on the vorticity transport equation (VTE) and the vortex identification method. Moreover, vibration signals are widely used to predict and diagnose pump faults. As cavitation develops, the random formation and rapid collapse of the cavitation bubble can cause the pump to vibrate unsteadily.[21,22] Al-Obaidi *et al.*[23,24] demonstrated that the vibration signal's peak, root mean square, crest factor, and spectrum can efficiently detect the incipient and development of cavitation. Zhou *et al.*[25] investigated the effect of vibration measurement point distribution on cavitation fault diagnosis. They concluded that the vibration signals on the inlet flange and pump body are more sensitive to cavitation. Luo *et al.*[26] proposed that mechanical seal wear causes a high-frequency vibration signal in pumps, and the energy of the vibration signal is related to the operating condition. The unstable flow induces a stronger vibration when the flow rate is low.

The natural flow of pumps is a particular condition applied in military vessel cooling systems, yet there is limited literature on the stall vortex features and the vibration mechanism under natural flow conditions. It is worth noting that the internal stall vortex features have a direct impact on the flow state of the cooling system's pump and have a close correlation with the pump set vibration, which, in turn, significantly affects system noise. Therefore, this work combined experimental measurements and numerical simulations to investigate the stall vortex and vibration characteristics of a multi-stage pump operating under natural flow conditions. The formation and motion characteristics of the stall vortex were studied using the Q-criterion and the vorticity transport equation. Furthermore, the experimental vibration signals were processed and analyzed using the empirical mode decomposition with singular value decomposition (SVD-EMD) and wavelet analysis methods. A detailed analysis was conducted on the low-frequency vibration characteristics resulting from stall vortices and unsteady flow. The results of this study provide significant theoretical support and technical guidance for improving the performance of circulating pumps in vessel cooling systems. This research offers insights into reducing equipment vibration and noise, and extending the service life of the equipment.

II. EXPERIMENTAL AND NUMERICAL SIMULATION STRATEGIES

A. Research subject

This study utilized a two-stage pump with guide vanes as the subject of investigation. The pump's design parameters include head of $H_d = 20$ m, flow rate $Q_d = 82\ m^3/h$, rated rotational speed $n_d = 960$ r/min, and specific speed $n_s = 94$. For each stage of the pump, an identical impeller and guide vane structure was employed, with the number of impeller blades $Z_1 = 3$, the blade wrap angle $\varphi_1 = 110°$, the number of guide vanes $Z_2 = 4$, and the guide vane wrap angle $\varphi_2 = 80°$. The impeller and guide vane were made of polymethyl methacrylate (PMMA), which exhibits reliable chemical properties and outstanding mechanical characteristics, as shown in Figs. 1(a) and 1(b). The three-dimensional structure assembly diagram of the pump is presented in Fig. 1(c) for reference.

B. Experimental method and signal processing method

1. Natural flow experimental equipment

The experimental equipment comprises a tested main pump, auxiliary pump, circulation piping system, and data acquisition system, as shown in Fig. 2. The schematic diagram of the control system

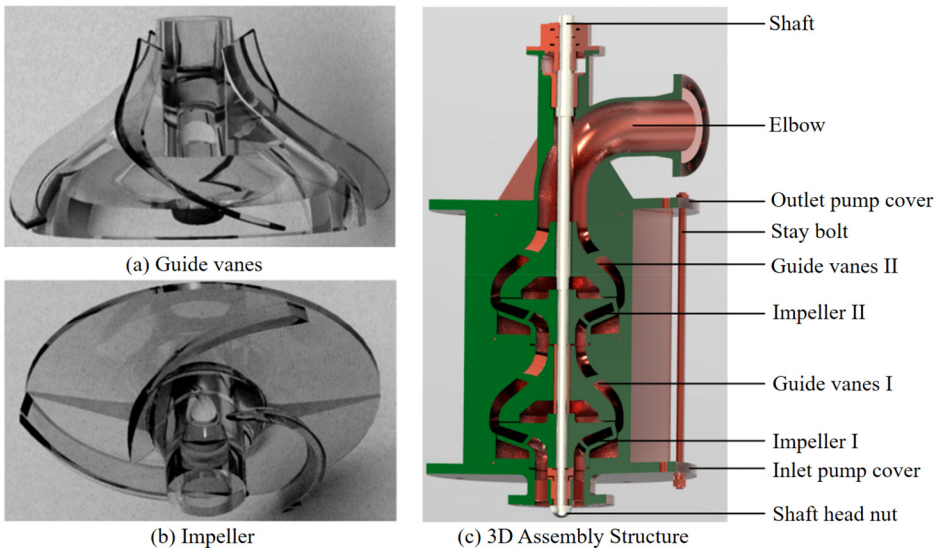

FIG. 1. Pump model structure.

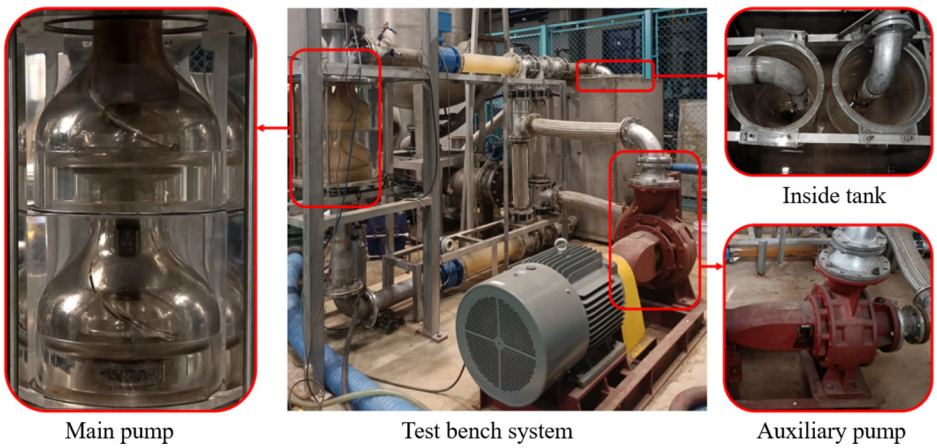

FIG. 2. Actual experimental system.

is displayed in Fig. 3. To simulate the impact of natural flow on the main pump, an auxiliary pump was employed as a booster device in the experimental system. The system's flow rate was controlled by adjusting the frequency of the auxiliary pump motor and the opening of the outlet valve. The pump's rotational speed, inlet and outlet pressure, and vibration signals were recorded at different flow rates. A PDH200–55 horizontal pump was selected as the booster equipment to achieve the maximum flow rate for the experiment, with a rated flow rate of 250 $m^3\ h^{-1}$, rotational speed of 1470 rpm, and power of 55 kW. This auxiliary pump was sufficient to provide stable energy for simulating the impact effects under diverse natural flow conditions.

The vibration signal acquisition system utilized INV9821 vibration acceleration sensors with a 10 mv/(m/s^2) sensitivity. The vibration acceleration was measured at two stages of the main pump and three times the pipe diameter of the inlet and outlet pipes, as illustrated in

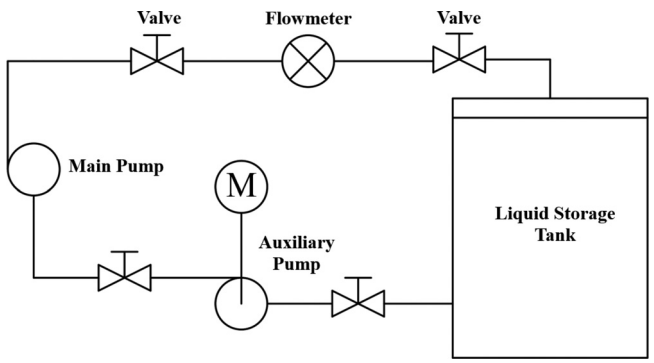

FIG. 3. Schematic diagram of system control.

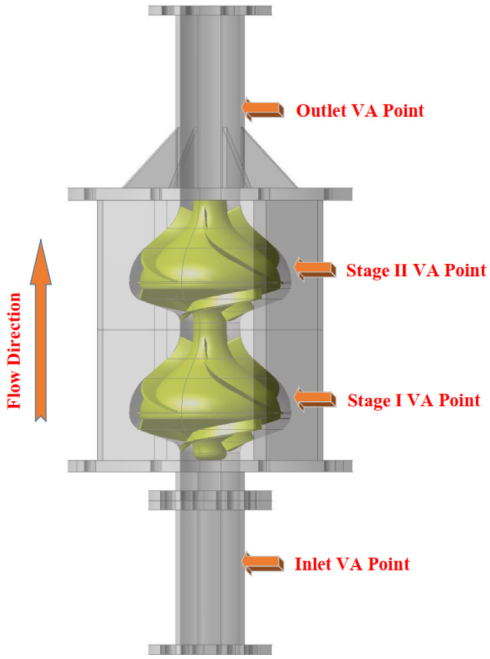

FIG. 4. Measurement points of vibration acceleration.

Fig. 4. Before the experiment, the mechanical seal cooling system of the main pump and the fan of the auxiliary pump motor were initiated. Furthermore, an inverter was employed to adjust the auxiliary pump motor's operating frequency, ensuring a stable and adequate power output to meet the maximum flow rate requirements. Additionally, potential experimental errors due to the adjustment of the auxiliary pump were minimized. The rated flow rate of the main pump under ordinary pump conditions $Q_d = 82\ m^3/h$ served as the reference standard. Sampling was conducted five times at 0.1 Q_d intervals from 0.1 Q_d to a maximum flow rate of 2.5 Q_d, with 1-min intervals between each sample. The sampling frequency of the vibration signal is 10 240 Hz, with each sampling lasting for 10 s.

2. Experimental reliability analysis

In this study, the hydraulic loss and rotational speed were used as benchmarks to assess the experimental accuracy. The uncertainty of the results under each condition was computed by Eq. (1) separately, and the average error of the entire experiment was determined to verify the reliability of the experimental results

$$\delta = \frac{\sqrt{\sum_{i=1}^{n}(x_i - \bar{x})^2}}{\bar{x}\sqrt{n}} \times 100\%, \tag{1}$$

where x_i means the experimental result of the ith measurement, $\bar{x}$ represents the average of the experimental results, and n denotes the number of repeated measurements. The error of hydraulic loss was calculated to be about ±0.281%, the passive speed of the impeller under natural flow condition was about ±0.497%, and the uncertainty of the experimental results was small and satisfied the accuracy requirement.

3. Vibration signal processing

The operation of the auxiliary pump generates vibration that transmits through the pipeline structure and fluid medium to the main pump, resulting in high noise interference in the sampled signal. In particular, the interference signal may obscure the characteristic components of the main pump signal in the high-frequency region, leading to inaccurate analysis results. Therefore, it is necessary to employ appropriate measures to mitigate the interference induced by the auxiliary pump's vibration before signal analysis.

Singular value decomposition (SVD) and empirical mode decomposition (EMD) methods were utilized to preprocess the sampled signals. Specifically, the SVD was used to reduce the interference of the auxiliary pump vibration signal. Then, the EMD method was employed to decompose the signal into a set of intrinsic mode functions (IMF), which significantly decreases mutual interference of signals in different spectrum bands, thus improving the pertinence and accuracy of signal analysis.

a. Singular value decomposition. Singular value decomposition (SVD) is a basic matrix decomposition technique that decomposes the feature components of a signal into different orthogonal subspaces. Assuming a real matrix A of order $N \times M$ with two orthogonal matrices $U \in R^{N\times N}$, $U \cdot U^T = I$ and $V \in R^{M\times M}$, $V \cdot V^T = I$, and a diagonal matrix $\Sigma = [\mathrm{diag}\{\sigma_1, \sigma_2, \ldots, \sigma_p\}:0]$, $p = \min(N, M)$. The singular value decomposition takes the following form:

$$A = U \sum V^T, \tag{2}$$

where U and V are orthogonal matrices of order $N \times N$ and $M \times M$, respectively, and set $\Lambda = \mathrm{diag}(\sigma_1, \sigma_2, \ldots, \sigma_p)$ be a diagonal matrix arranged in descending order, and elements on the diagonal are called singular values. The essence of SVD decomposition is to project matrix A into a series of uncorrelated subspaces. The number of singular values of the matrix reflects the number of independent row (column) vectors of the matrix, and all diagonal elements of the diagonal matrix are not zero when the noise exists.

b. Empirical mode decomposition. Empirical mode decomposition (EMD) is a signal decomposition method based on data-adaptive multiresolution techniques. It can decompose the nonlinear and nonstationary time-domain signal $x(t)$ into a superposition of a finite number of intrinsic mode functions (IMF). Each IMF reflects the local vibration pattern of the signal at different frequencies and time scales, thus providing a wealth of signal information. The expansion is as follows:

$$x(t) = \sum_{i=1}^{n} imf_i(t) + r_n(t), \tag{3}$$

where $imf_i(t)$ is the ith intrinsic mode function obtained from the EMD, and $r_n(t)$ is the trend term of the signal.

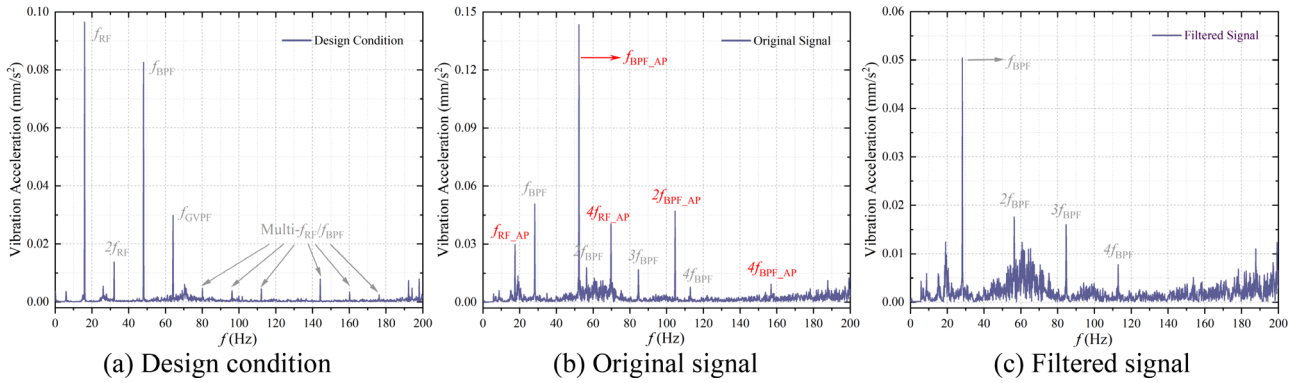

FIG. 5. Signal comparison.

Figure 5(a) displays the spectrum characteristics of the main pump under normal operating conditions, where the primary and secondary frequencies are at the rotational frequency $f_{RF} = 16$ Hz and the blade passing frequency $f_{BPF} = 48$ Hz, respectively. In addition, there is also a high amplitude at the guide vane passing frequency $f_{GVPF} = 64$ Hz, and the resonance appears at the multiples of the rotational frequency and the blade passing frequency. Figure 5(b) presents the original vibration signal collected under a natural flow condition of $2.0Q_d$. It can be observed that the peak at the blade passing frequency of the auxiliary pump f_{BPF_AP} is three times higher than that of the main pump. The amplitude at the rotational frequency f_{RF_AP} and its harmonics are also significantly higher than the nearby main pump signal. Consequently, some vibration signal characteristics of the main pump are overlooked in the spectrum analysis.

Based on the SVD method, it is possible to effectively filter out the noise signal caused by the auxiliary pump, as demonstrated in Fig. 5(c). It allows a more comprehensive capture of the vibration signal characteristics of the main pump under natural flow conditions. Furthermore, the comparison between the design and natural flow conditions reveals differences in the vibration signal characteristics. Under the design condition, the vibration signal energy is more concentrated at the f_{RF}, and the resonance frequency consists of multiple f_{RF}. However, under the natural flow condition, the characteristic frequencies are mainly at the f_{BPF} and its multiples, while the signal at the f_{RF} is not prominent.

The f_{BPF} generated by the rotor–stator interference is a primary source of pump vibration. Meanwhile, the vibration energy at the f_{RF} reflects the unbalance force induced by deformation and eccentricity of the shaft or impeller. The rotational frequency is more likely to appear when the pump is driven by a motor, while it is not as apparent under natural flow conditions.

C. Numerical simulation methods

1. Computational domain geometry

The computational domain of the main pump fluid body was established by Creo modeling software. Sufficiently lengthy pipelines were established at the inlet of the first-stage impeller and the outlet of the secondary guide vane to ensure adequate flow development. The three-dimensional computational domain of the main pump is shown in Fig. 6.

2. Grid generation

This study adopted ANSYS ICEM software to generate structured multi-block hexahedral grids for impellers, guide vanes, and inlet and outlet pipelines, as shown in Fig. 7. Due to the complex geometric features of pump components, multiple block splitting methods were employed to achieve the topology of the mesh structure. For the import and export channels, the "O" block method was employed. However, for complex computational domains such as impellers and guide vanes, it is necessary to first cut an individual flow channel. Then, topology is established by stretching, splitting, and "Y" blocking. The refinement of specific regions, such as blades, gaps, and boundary layers, was carried out based on geometric features to ensure that the maximum y+ value was less than 80. Based on the same grid topology and with high-quality grid, five different sets of grids were established for grid independence verification, as shown in Fig. 8. The error of hydraulic loss under natural flow conditions is less than 2% as the judgment criterion, and grid case 3 is finally selected as the simulation grid.

3. Boundary conditions

The ANSYS CFX commercial code was utilized to simulate the flow field characteristics under different natural flow conditions. The shear stress transport (SST) k–ω model was used to describe the turbulent flow. The fluid medium was clean water at 25 °C, with a relative reference pressure of 0. The inlet was set as pressure-inlet, and the outlet was mass-flow. The rotational speed was set according to the experimental measurements obtained under different natural conditions. The impeller blades, shroud, and hub were set up as rotating walls, and the rest as non-slip walls. The general grid interface (GGI) method was

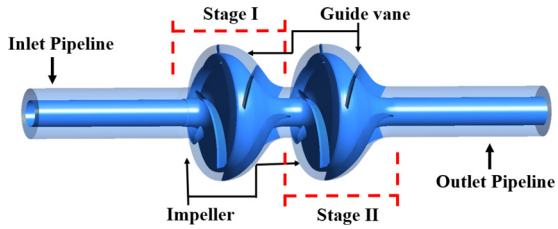

FIG. 6. Computational domain of main pump.

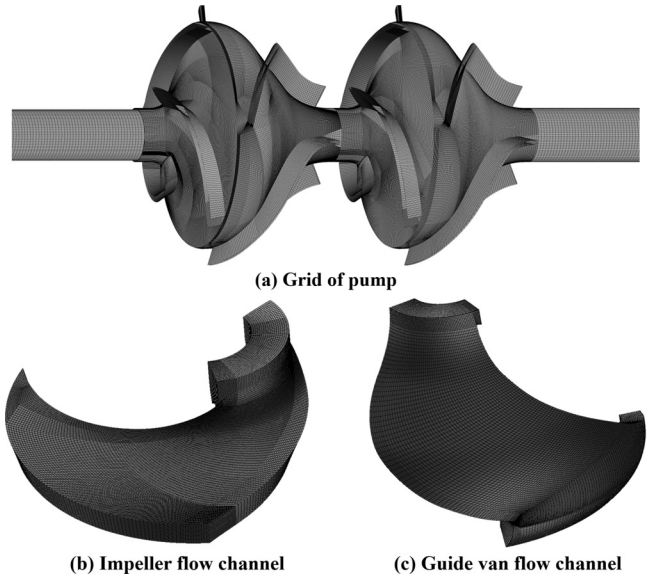

FIG. 7. Computational domain grid.

adopted to define the dynamic and static domains interface. The total time was 1.0 s, and the time step was 2×10^{-4} s. The maximum iteration per time step was set to 10, and the convergence criterion was set to 10×10^{-6}.

III. ANALYSIS AND DISCUSSION OF RESULTS

A. Accuracy verification

Figure 9 illustrates the trends in rotational speed and hydraulic losses with varying flow rates under natural flow conditions and compares the errors between the hydraulic losses obtained from numerical simulations and experimental measurements. Notably, the numerical

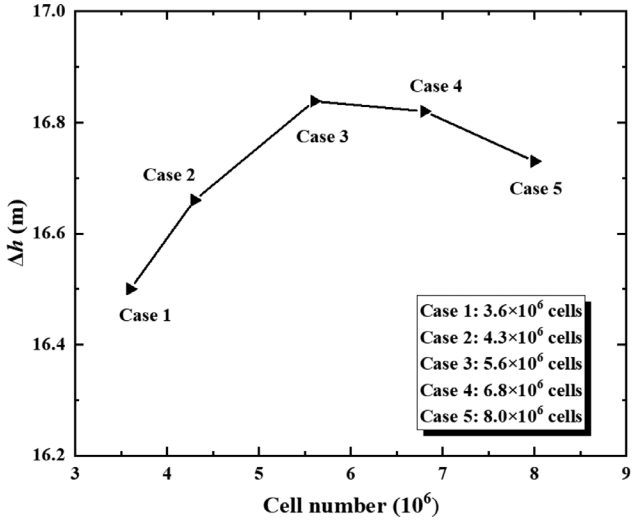

FIG. 8. Grid independence verification.

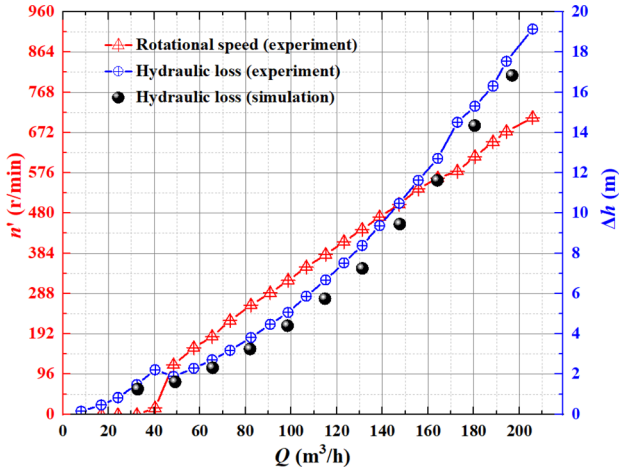

FIG. 9. Variation of hydraulic loss and rotational speed.

simulation neglects the volumetric losses, mechanical friction losses, and heat transfer losses in the experimental measurements, leading to relatively low results than the experiments. However, the average error is within 8%, which is comparatively low. The variation trend remains consistent, and the hydraulic loss increases exponentially with the flow rate. In addition, the impeller is stuck when the flow rate is below 32 m^3/h. The force of the incoming flow on the impeller is insufficient to make the impeller overcome the mechanical resistance and rotate passively. When the flow rate is higher than 48 m^3/h, the rotational speed increases linearly with the flow rate.

B. Analysis of stall vortex characteristics

The generation mechanism of stall vortex in rotating machinery is a complex phenomenon influenced by various factors, including blade geometry, rotational speed, flow rate, and blade attack angle. One significant factor to stall vortex is the increase in the inlet attack angle and the flow separation phenomenon on the blade surface. Under ordinary pump conditions, the impeller speed remains stable, and the circumferential velocity w inside the impeller remains relatively constant. However, if the flow rate falls below the design condition, the relative inlet velocity v decreases, resulting in an increase in the attack angle between the combined velocity c and the inlet blade edge. When the attack angle reaches a specific value, flow separation and stall vortex will be formed near the blade surface, as shown in Fig. 10(a).

Under natural flow conditions, the impeller rotates passively due to the impact of natural flow, and its rotational speed increases linearly with the flow rate. The relative inlet velocity v and circumferential velocity w compose a similar triangle of velocity vector. Consequently, the inlet attack angle of the blade remains constant at different flow rates, as illustrated in Fig. 10(b).

Under natural flow conditions, the two-stage pump is prone to generating stall vortex, leading to a decline in hydraulic performance. This phenomenon increases the flow resistance and produces detrimental vibration and noise. The effects of stall vortex on the performance curve differ significantly from that of the pump under ordinary operating conditions. To illustrate this, Fig. 11 compares the

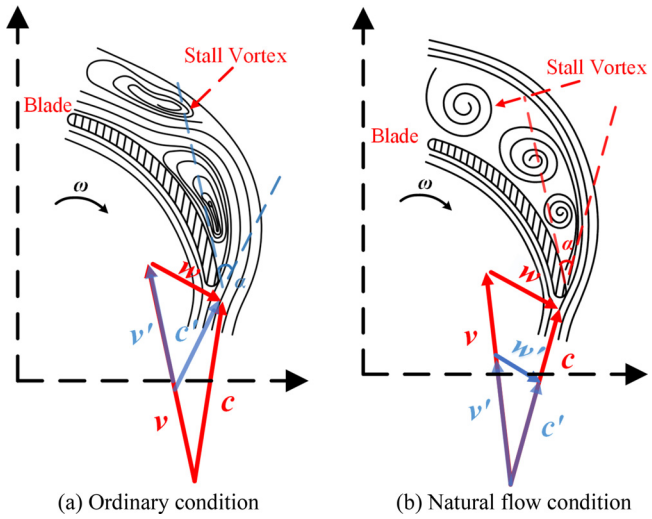

FIG. 10. Principle of stall vortex generation.

streamline characteristics inside the impeller at various flow rates. Under the ordinary condition, although vortexes exist on the blade pressure side in some partial impeller channels, the vortex sizes are relatively small, and the structure is stable. It does not obstruct the flow channel causing severe hydraulic losses.

Under natural flow conditions, the impeller motion can be classified into two modes: stuck and passive rotation. As shown in Fig. 11(b), when the flow rate is less than $0.4Q_d$, the force exerted by the incoming flow on the impeller is insufficient to overcome the mechanical impedance, causing the impeller to remain stationary. The fluid flow into the impeller lacks circumferential velocity and flows along the blade suction side toward the impeller outlet. Due to the mismatch between the inlet liquid flow angle and the blade angle, a larger area of stall vortex forms at the blade pressure side. Additionally, the stall vortex structure is unstable and influenced by the high velocity–pressure difference in the impeller flow channel. It undergoes a cyclic process of initiation, splitting, and integration within a rotation cycle. However, when the flow rate exceeds $0.4Q_d$, the impeller rotates passively, and its rotational speed increases linearly with the flow rate. Therefore, the blade attack angle remains almost constant at different flow rates, resulting in similar streamline figures at various flow rates. Figures 11(c) and 11(d) present that the stall vortex regions under natural flow conditions of $1.0Q_d$ and $2.0Q_d$ are mostly the same, consisting of stall cells with different scales and directions. These stall cells primarily gather near the blade leading edge. It is noteworthy that there are significant distinctions in the internal flow patterns of the first-stage and second-stage impellers under ordinary conditions, with larger vortex scales on the blade pressure side of the first-stage impeller. However, under natural flow conditions, there are greater similarities between the impellers of both stages.

The flow instability and related factors lead to the formation of various scales and directions vortex in the pump under natural flow conditions. The vortex identification theory is based on the velocity and pressure gradient of the fluid. The *Q*-criterion is a widely used application of vortex identification theory, defined as follows:

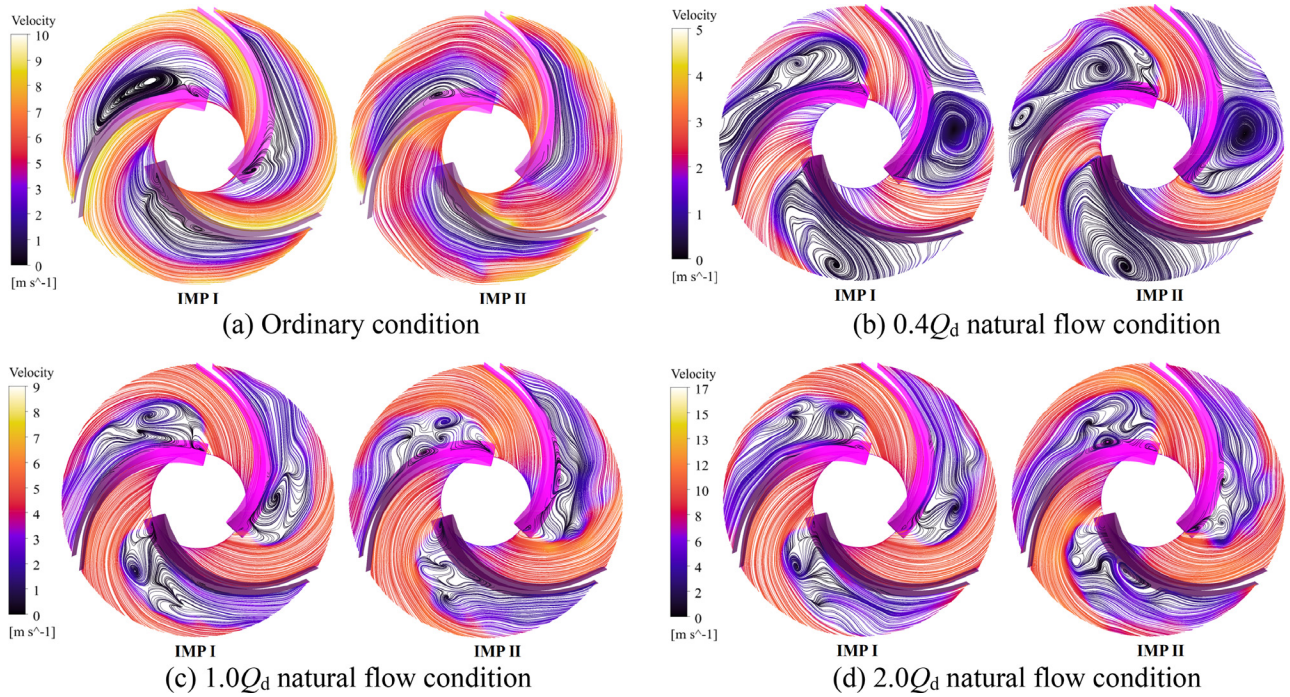

FIG. 11. Streamlines under different conditions.

$$Q_c = -\frac{1}{2}(S_{ij}S_{ij} - \Omega_{ij}\Omega_{ij}), \tag{4}$$

where S_{ij} is the strain rate tensor and Ω_{ij} is the vorticity tensor, respectively, defined as

$$S_{ij} = \frac{1}{2}\left(\frac{\partial u_i}{\partial x_j} + \frac{\partial u_j}{\partial x_i}\right), \tag{5}$$

$$\Omega_{ij} = \frac{1}{2}\left(\frac{\partial u_i}{\partial x_j} - \frac{\partial u_j}{\partial x_i}\right). \tag{6}$$

In the Q-criterion, a positive value of Q_c indicates a region in the flow field where the vorticity dominates. In contrast, a negative value indicates that the strain rate or viscous force dominates.

Figure 12 shows the distribution of the internal vortex structure for the natural flow conditions of $0.4Q_d$, $1.0Q_d$, and $2.0Q_d$, and compares it with the ordinary condition. The internal vortex structure and motion track inside the impeller evolve under different conditions. In the ordinary condition, the center of the first-stage impeller channel has a stable primary passage vortex that extends from the inlet to the outlet, with a small amount of vortex shedding near the impeller outlet. The second-stage blade inlet exists more intensive vortex mass, with the primary vortex flowing toward the blade's suction side. Additionally, significant tip leakage vortex is observed at the impeller outlet.

Under the natural flow condition of $0.4Q_d$, the impeller remains in a stuck state, leading to a significant deviation in the inlet angle of attack from the design, resulting in a more intricate vortex structure. The stall vortex, generated by flow separation, may obstruct a portion of the flow channel, resulting in the formation of numerous small-scale split vortex at the blade's leading edge. Moreover, the movement toward the impeller outlet may induce low-frequency oscillations. A stable stretched vortex also exists near the impeller suction side, while some small-scale vortex masses merge within the second-stage impeller.

Under the natural flow condition of $1.0Q_d$, the impeller takes passive rotation in response to the flow impact, and the internal vortex be primarily distributed on the blade pressure side. The stall vortex is shed into multiple cells of different scales flowing downstream. Furthermore, due to the influence of outlet rotor–stator interference, more intricate tip leakage vortex is observed. As the flow rate rises, the stall vortex mass gathers at the 1/2 blade pressure side at a flow rate of $2Q_d$, obstructing the impeller flow channel. The vortex evolution inside the second stage becomes more complex, involving processes of vortex decay, splitting, merging, and development.

C. Mechanism of stall vortex generation

To further investigate the mechanism of stall vortex generation inside the pump under natural flow conditions, and estimate the incipient, developmental, and dissipation stages of the stall cell, this work employed the vorticity transport equation to investigate the direct interaction between the stall vortex and the internal structure of the pump, which is expressed as follows:

$$\frac{D\vec{\Omega}}{Dt} = (\vec{\Omega}\cdot\nabla)\vec{V} - \vec{\Omega}(\nabla\cdot\vec{V}) - 2\nabla\times(\omega\times\vec{V}) + \frac{\nabla\rho_m\times\nabla p}{{\rho_m}^2} + \nu\nabla^2\vec{\Omega}, \tag{7}$$

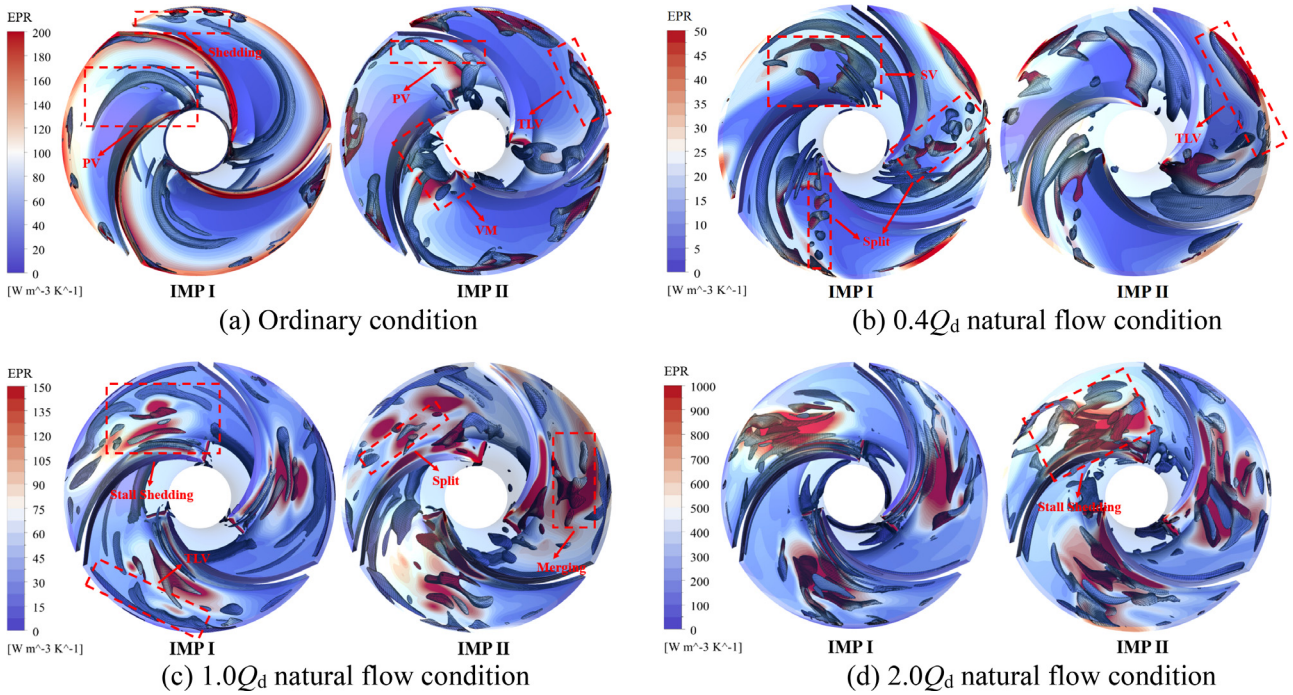

FIG. 12. Vortex features under different conditions.

where $\vec{\Omega}$ represents the vorticity, $\vec{V}$ denotes the relative velocity of the flow field, ω stands for the rotational angular velocity, and ν represents the fluid kinematic viscosity. The formation of vorticity involves five main terms. The first of term is the vortex stretching (VS) term, characterizing the stretching and tilting of the vortex caused by the velocity gradient. The second term represents the vortex dilatation, reflecting the effect of fluid compressibility on the vortex volume. The third is the Coriolis force (CF) term, which describes the contribution of the inertial forces within the reference frame of impeller rotation. The fourth term is the baroclinic torque term, which indicates the variation of the vortex caused by the deviation of the pressure gradient and the density gradient of the medium. The last term is the viscous dissipation (VD) term, primarily influenced by the viscous dissipation of the fluid. However, in the case of considering the medium as an incompressible fluid, the effects of the vortex dilatation and the baroclinic torque terms are neglected.

In this study, three typical sets of natural flow conditions, $0.4Q_d$, $1.0Q_d$, and $2.0Q_d$, were selected to investigate further the influence characteristics of vortex stretching, Coriolis force, and viscous dissipation on the stall vortex evolution of pumps based on the vorticity transport equation. The Span coefficient defines the dimensionless distance (from 0 to 1) between the shroud and the hub of the impeller. A smaller value of the Span coefficient indicates closer proximity of the surface to the impeller hub and the guide vane inner wall. Blade-to-blade surfaces with Spans of 0.01 (near the hub), 0.2, 0.5, 0.8, and 0.99 (near the shroud) were established to further analyze the mechanism of vortex generation under natural flow conditions. The position of blade-to-blade surfaces is shown in Fig. 13.

Figure 14 shows the influence of the vortex stretching on the vortex field under different natural flow conditions. The distribution of the local high VS region is primarily affected by the internal stall vortex structure and velocity gradient, resulting in noticeable variations. At a flow rate of $0.4Q_d$, the high VS region is mainly concentrated at the leading edge of the blades at each stage, specifically at a Span of 0.01 and 0.2 blade-to-blade planes. It then extends along the pressure side toward the outlet and accumulates at impeller and guide vane clearance. As the impeller is in a static state, the liquid flow leaving the impeller shocks the backside of the guide vane, causing the formation of a large-scale stall vortex in the guide vane flow channel near the working surface. Consequently, the high VS region is mainly located near the guide vane's backside and the stall vortex's outer ring. At a Span of 0.5, VS is chiefly distributed in the blade flow separation and tip clearance. Additionally, at Spans of 0.8 and 0.99, a high VS region appears near the suction side of the first-stage impeller blade. This region exhibits a relatively stable band-shaped distribution and extends into the guide vanes. The VS distribution in each channel of the second-stage impeller shows some variations, but the pattern is similar to that of the first stage.

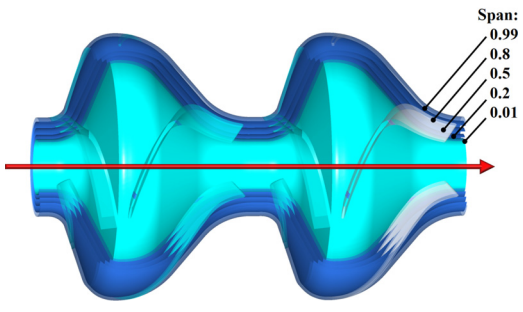

FIG. 13. Position of blade-to-blade surface.

Under the conditions of $1.0Q_d$ and $2.0Q_d$, the inlet flow angle is similar, resulting in comparable features of the internal flow field, with the primary difference being in the magnitude of velocity and pressure. At a Span of 0.01 and 0.2, the high VS region is mainly distributed near the blade's leading edge and pressure side of the first stage, extending to the 1/2 channel of the impeller. The high VS region at the inlet of the second-stage impeller splits during the flow downstream, coinciding with the disruption region of the vortex core. The distribution is more uniform in the guide vane flow channel, but high VS exists near the flow separation and the trailing edge. At a Span of 0.5, 0.8, and 0.99, the high VS is primarily located near the leading edge of the blade and the region of the stall vortex dynamic separation. With an increase in flow rate, the region of local high VS between the impeller and guide vane expands, and the intensity of tip leakage vortex becomes relatively stronger. The distribution of VS effectively reflects the primary characteristics of the formation and evolution of stall vortex and tip leakage vortex. Furthermore, the stretching and bending of the vortex structure inside the pump are the fundamental reason for the variation of vorticity.

Figure 15 illustrates the effect of the Coriolis force on the vorticity field inside the impeller for $1.0Q_d$ and $2.0Q_d$ natural flow conditions. Since the Coriolis force is related to the rotational motion and the impeller is stationary at $0.4Q_d$, the Coriolis force has no effect in this case. The high CF region is closely associated with the stall vortex structure within the impeller. At a flow rate of $1.0Q_d$, a high CF region is observed at the blade leading edge and pressure side at a Span of 0.01, with small-scale stall cells appearing at the outlet of the second-stage impeller. At a Span of 0.2, a large-scale vortex emerges near the blade pressure side and within the flow channel of both stages. The high CF region in the first stage is primarily distributed in the wake region of the stall vortex. In contrast, in the second stage, it is primarily distributed on the pressure side of the front half of the blade, with partial splitting in the wake and dissipation toward the outlet. At Span of 0.5, 0.8, and 0.99, the high CF region is located in the flow separation at the leading edge of the blades. When the flow rate rises to $2.0Q_d$, the relatively high CF region expands and tends to move toward the shroud. The pattern of high CF within the impeller exhibits similarities at both stages. In the state of impeller passive rotation, the Coriolis force analysis can effectively reflect the internal structure and motion characteristics of the stall vortex.

Figure 16 shows the distribution characteristics of the viscous dissipation term. The generation of viscous forces is attributed to the interaction between turbulent flows and is closely linked to the evolution and interference of the stall cells. Moreover, the dissipation of the stall cell is caused by the viscous shear force, leading to the inhibitory effect of the viscous force on vortex evolution. At the operating condition of $0.4Q_d$, the regions with high VD are mainly located near the blade inlet, flow separation region, tip clearance region, and high velocity gradient region at the back of the second-stage guide vanes. These regions also exhibit high VD in the $1.0Q_d$ and $2.0Q_d$ flow conditions. Moreover, when the impeller undergoes passive rotation, discrete regions with high VD also appear inside the stall vortex and in

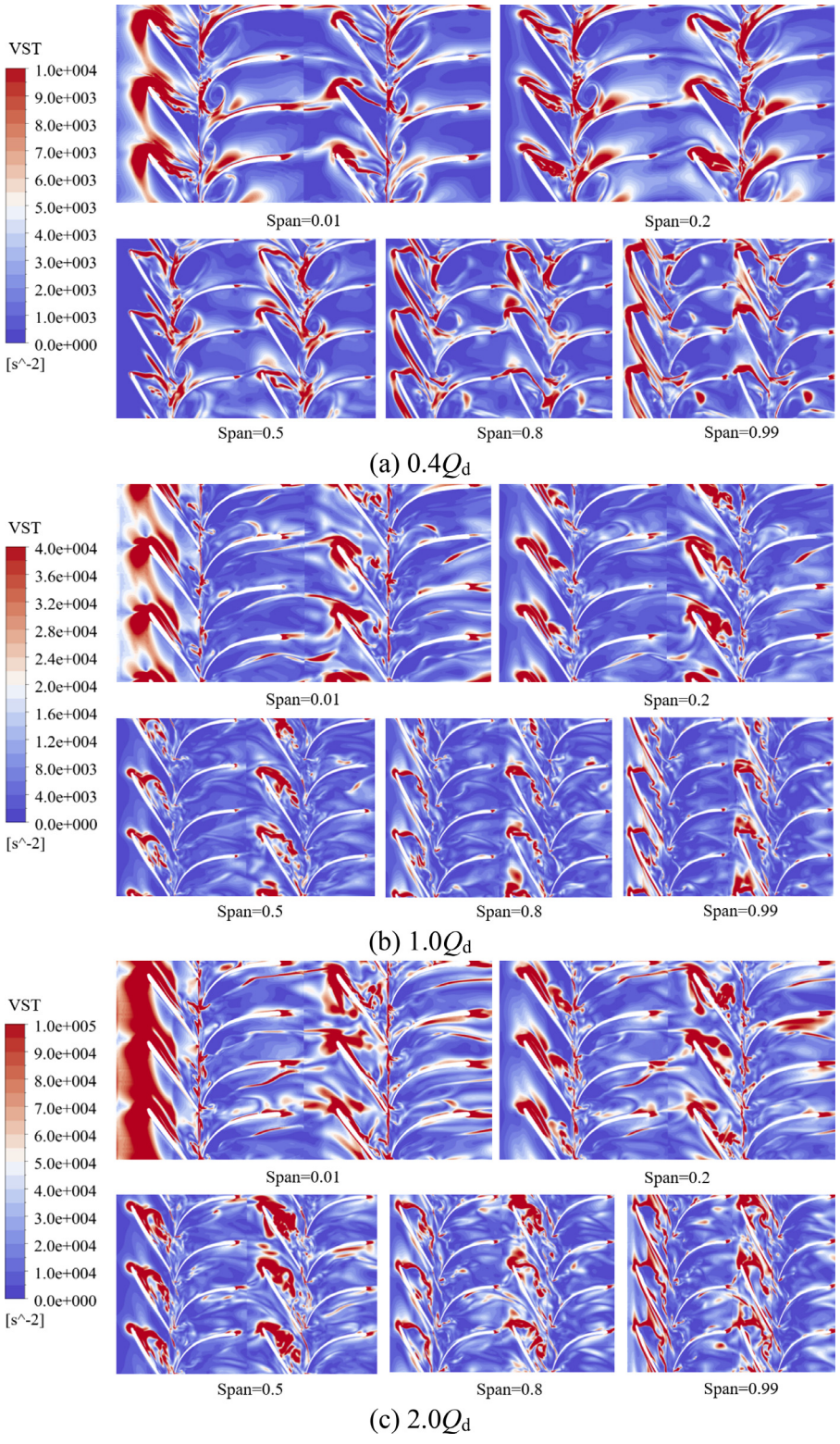

FIG. 14. Effect of the vortex stretching term.

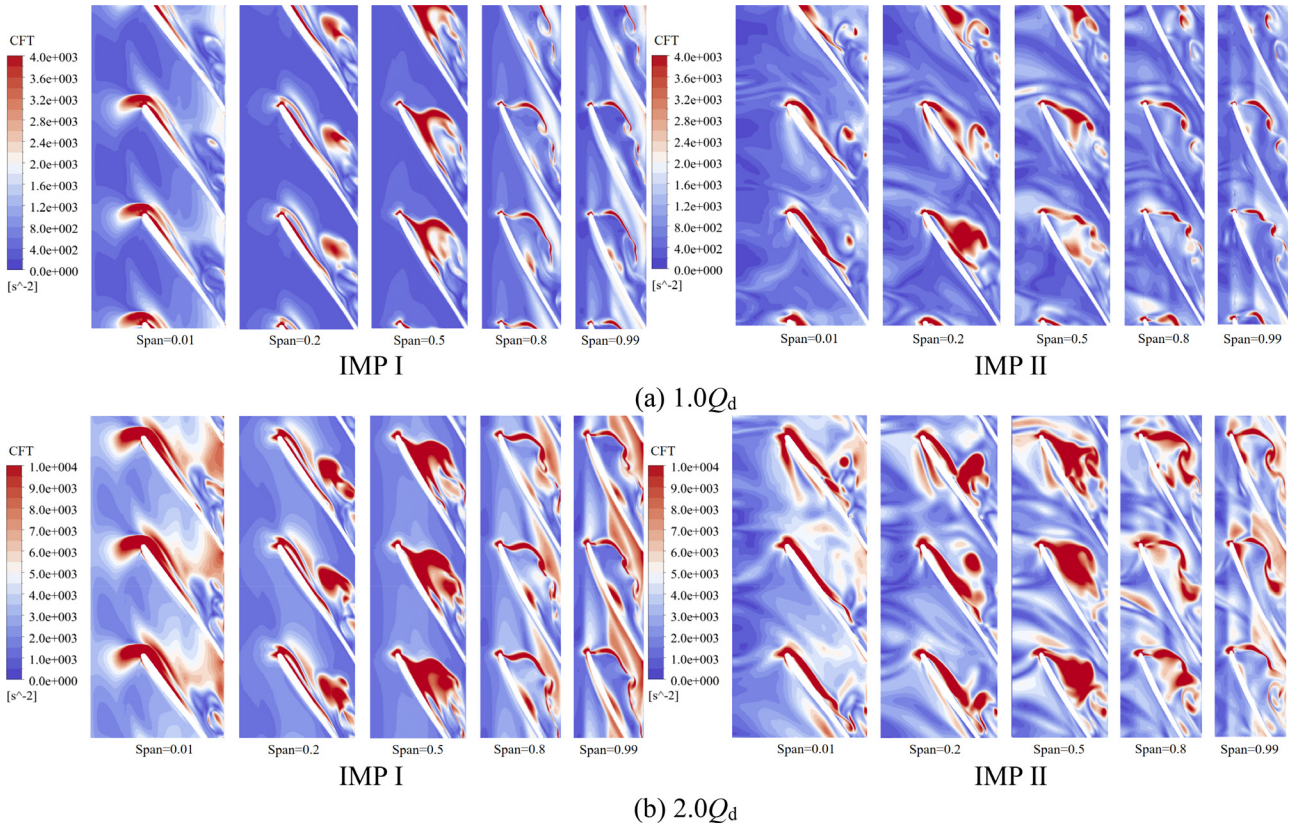

FIG. 15. Effect of the Coriolis force term.

the wake. These regions indicate the energy dissipation generated by friction and viscous effects in stall cells of different scale. Although the value of the viscous dissipation term in the natural flow condition is relatively small, its effect on the vorticity field should not be disregarded. Meanwhile, a relatively strong correlation exists between the viscous force and the evolution of the vortex.

D. Excitation force characteristics analysis

Figure 17 shows the variation of the axial excitation force under different natural flow conditions. Overall, the axial excitation force of the two-stage impellers exhibits a gradual increase as the flow rate rises. The first-stage guide vane (Gui I) experiences a slight increase in axial excitation force, while the second-stage guide vane (Gui II) shows a significant decreasing trend. At flow rates ranging from $0.4Q_d$ to $1.2Q_d$, the axial force on the first-stage impeller (Imp I) is the highest, and the axial force on the second-stage impeller (Imp II) is slightly lower than Imp I, with the difference between both is gradually decreasing. Specifically, at a flow rate of $0.4Q_d$, the axial force of Imp I is 3.8% higher than that of the second stage, while at a flow rate of $1.2Q_d$, it is only 0.43% lower. For flow rates higher than $1.4Q_d$, the axial force on Imp II gradually exceeds that of Imp I. Meanwhile, the difference between both stage guide vanes also increases significantly. At a flow rate of $2.4Q_d$, the axial force on Imp II is 5.2% higher than that of the first stage, while the axial force on Gui II is relatively reduced by 35.4%.

This phenomenon can be attributed to the effect of natural flow shock on the axial forces of the components under low flow rates. The first-stage experiences a large shock force from the incoming flow while buffering the second-stage components, resulting in a relatively smaller axial excitation force. Moreover, at high flow rates, the flow state inside the pump deteriorates stage by stage due to the impeller speed and flow rate not matching the design situation. The stall vortex and backflow phenomenon in the flow channel of the second-stage impeller are intensified, and the turbulent kinetic energy is increased, which leads to the increase in the axial force.

Figure 18 shows the variation of the radial excitation force of the impeller and guide vane at each stage with flow rate. The radial excitation force of each component increases with the flow rate rises. However, the total radial force for each component remains relatively small, reaching a maximum of about 26 N. At a flow rate of $0.4Q_d$, the impeller is stationary, and the radial force shows an increasing trend from Imp I to Gui II. The radial force of Gui II is approximately 2.5 times higher than that of Imp I.

When the flow rate is between $0.6Q_d$ and $1.4Q_d$, the impeller begins to rotate passively due to the impact of the incoming flow, and

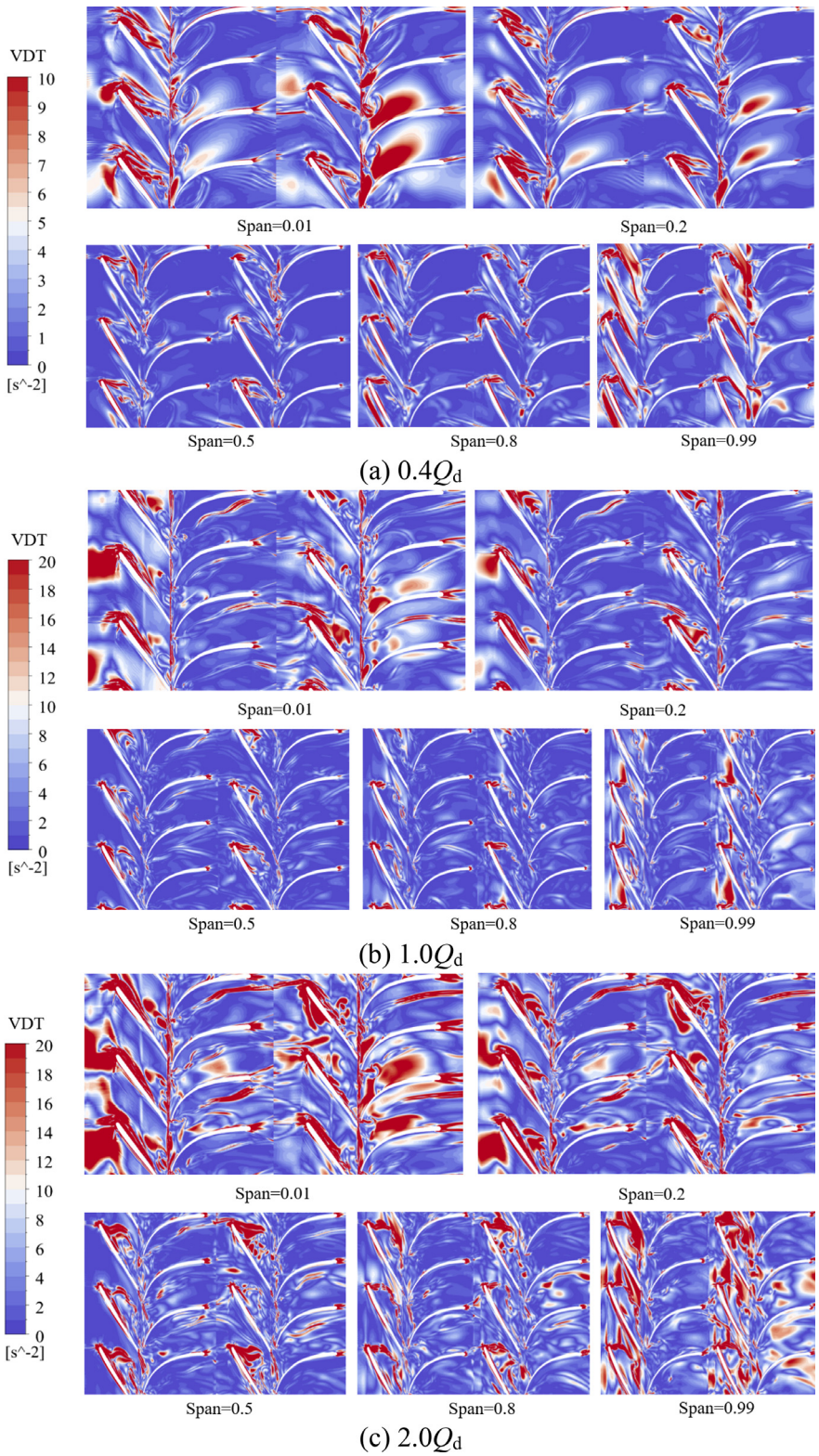

FIG. 16. Effect of the viscous dissipation term.

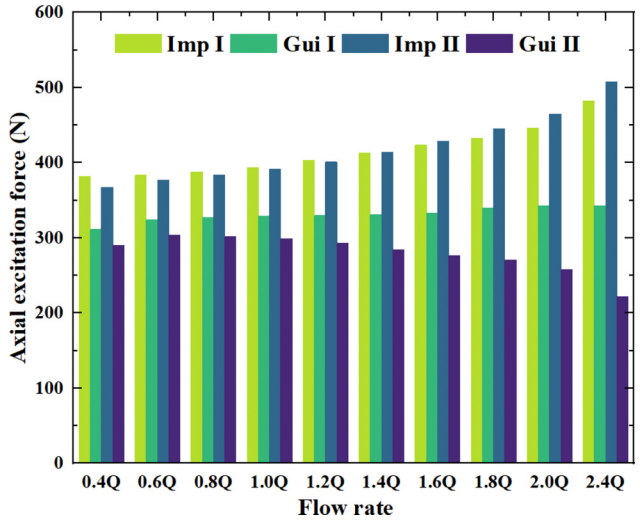

FIG. 17. Variation of axial excitation force at different flow rates.

its rotational speed increases continuously. The radial force of the second stage is higher than that of the first stage, and the radial force on Imp II is the largest. However, the difference between the two stages gradually decreases. At a flow rate of $0.6Q_d$, the radial forces of Imp II and Gui II are about twice as high as those of the first stage. While at a flow rate of $1.4Q_d$, the radial force of Imp II rises by 37.8%, and Gui II increases by only 11.9%. For flow rates higher than $1.6Q_d$, the radial excitation force on Gui II starts to be lower than that of the first stage, and the radial force difference becomes more pronounced as the flow rate rises. At $2.4Q_d$, the radial force on Gui II decreases by about 14.3% compared to the first stage.

The main reason for this phenomenon is that the radial excitation force is generated from the static pressure at the wall and the

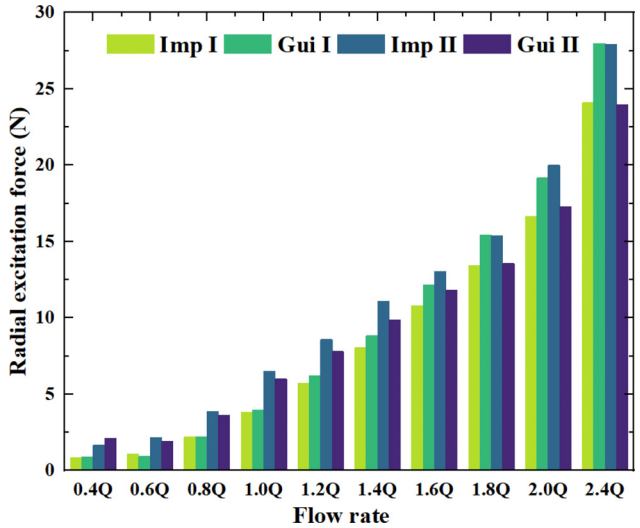

FIG. 18. Variation of radial excitation force at different flow rates.

dynamic pressure caused by the turbulent flow. The static pressure at the wall decreases stage by stage due to increased flow loss, while the dynamic pressure increases by stage, influenced by the rise of turbulent kinetic energy. At low flow conditions, the effect of turbulent kinetic energy on the radial excitation force dominates, resulting in a higher radial force on Gui II compared to the first stage. Under high flow conditions, the influence of wall static pressure is stronger, and the increase in radial force caused by turbulent kinetic energy is relatively small. Therefore, the radial force on Gui I is more significant. In addition, the turbulent kinetic energy within the impeller is more intense compared to the guide vane, and the difference of wall static pressure between the two-stage impellers is lower, making the radial force of Imp II consistently higher than that of the first stage.

Figure 19 displays the spectral characteristics of the radial excitation force generated by impellers and guide vanes at different stages under different natural flow conditions. Due to the passive rotation of the impeller under the impact of the incoming flow, the energy signal is primarily composed of the stall vortex frequency and the blade passing frequency (BPF). Thus, the characteristic frequency is mainly concentrated in the low frequency.

At a flow rate of $0.4Q_d$, the impeller is stationary. The radial excitation energy is mainly concentrated within the 40 Hz frequency range. The magnitude of this energy reflects the intensity of stall vortex frequency at different scales. The overall performance exhibits a broadband feature. As the flow rate increases, the fluid flow drives the impeller to rotate passively, and the spectrum of the radial excitation force shows prominent discrete characteristics. The radial forces on the impeller and guide vane exhibit some diversity in the y and z directions. The main frequency inside the impeller is the guide vane passing frequency (GVPF), and the second frequency is twice GVPF. In contrast, the main frequency inside the guide vane is the blade passing frequency (BPF), and there are harmonics at triple BPF.

The above phenomenon is primarily attributed to the rotor–stator interference. During one rotation cycle of the impeller, each guide vane rotates relative to the static impeller for one cycle. As a result, four guide vanes interact with each blade four times, transmitting pulsations to the impeller and producing the main frequency of GVPF. Similarly, the generation of the characteristic frequency on the guide vane can be explained. The main frequency of total radial excitation force occurs at the quadruple BPF (triple GVPF), representing the harmonic frequency between BPF and GVPF.

E. Vibration characteristics analysis

In order to better analyze the variation of vibration intensity with flow rate under natural flow conditions, it is necessary to consider the significant difference in vibration acceleration between low and high flow rates. Therefore, this study introduces the vibration acceleration level (VAL) to evaluate the average energy of vibration, which allows a more intuitive comparison of vibration levels at different measuring points at different flow rates. The expression for the VAL is as follows:

$$VAL = 10\lg\frac{\sqrt{\frac{1}{N}\sum_{n=1}^{n}|a_n|^2}}{a_0}, \tag{8}$$

where a_n is the vibration acceleration value of the nth time point, n is the total number of sampling points, and a_0 is the reference vibration

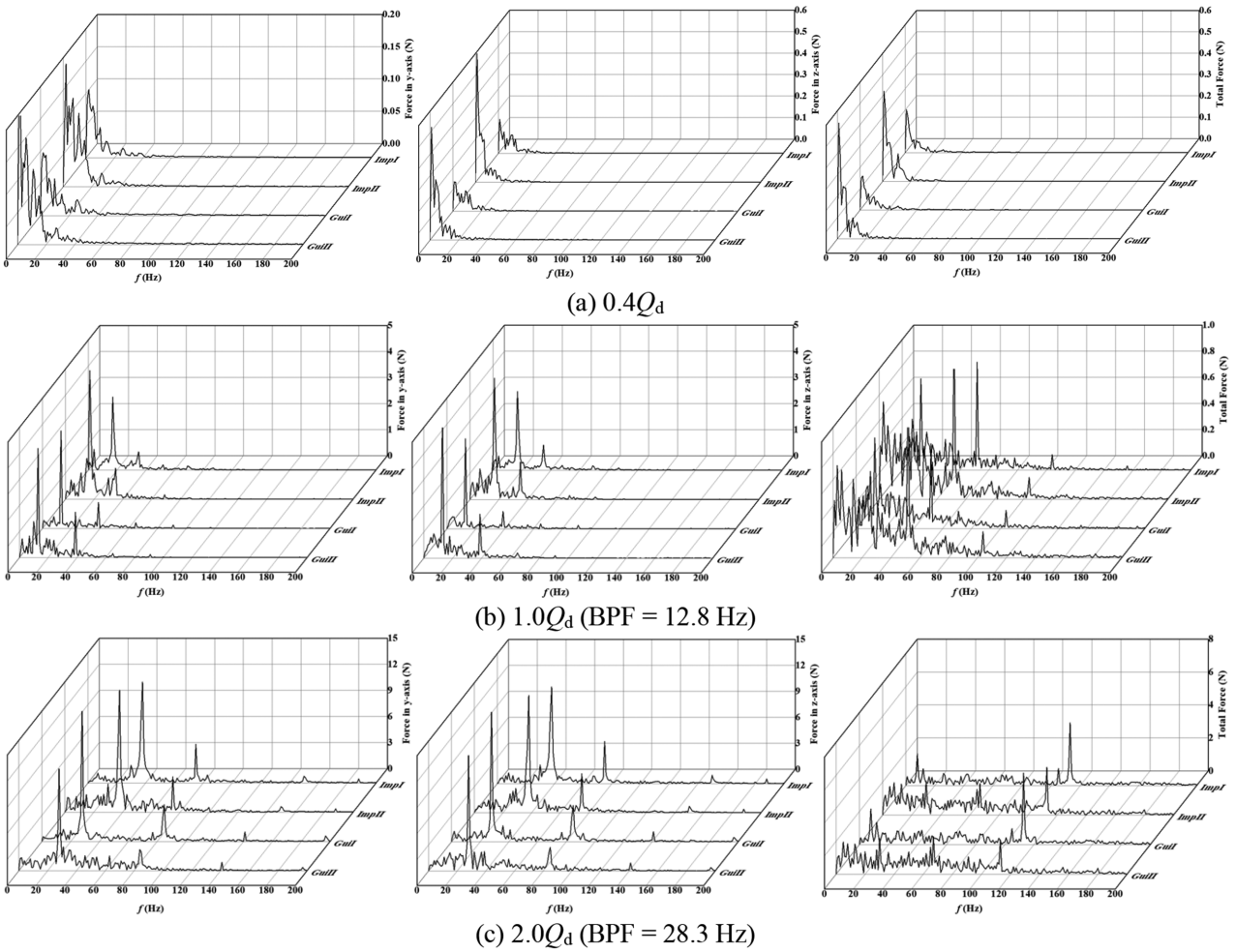

FIG. 19. Radial excitation force spectrum characteristics.

acceleration, which is 1×10^{-6} m/s^2. The VAL reflects the energy level of the vibration signal, and its higher value indicates the higher energy level of the vibration signal.

Figure 20 illustrates the variation of the VAL at each experimental measuring point under different natural flow conditions. For the 0–0.5Q_d condition, the average VAL initially increases and then decreases. However, for flow rates ranging from 0.5–2.5Q_d, the VAL rises continuously with an overall increment of about 35 dB. Additionally, for each 0.1Q_d increase in the average flow rate, the VAL increases by 2.5 dB.

At flow rates below 1.4Q_d, the pump components' contribution to the VAL is ordered as follows: first-stage pump, outlet pipe, inlet pipe, and second-stage pump. Nevertheless, when the flow rate exceeds 1.4Q_d, the contribution of the pump components undergoes a significant change. Specifically, the second-stage accounts for the largest proportion, followed by the first-stage pump, while the inlet and outlet pipes contribute equally. As the flow rate increases, a distinct correlation arises between the vibration of the two stages and the axial excitation force. The internal flow and operating conditions of the pump significantly affect the intensity of the vibration. The increase in flow rate produces more shock force, resulting in increased turbulence and pressure pulsation, which in turn causes more intense unsteady excitation force acting on the hydraulic components. Moreover, the rotor–stator interference increases as the rotational speed rises, which is a crucial factor for the increased vibration.

Since the original signal spectrum of vibration under natural flow conditions is almost covered by broadband signals, except for the main frequency signal and the first few orders of sub-frequency signals, the EMD method was utilized to decompose the vibration signal. The first 15 IMF components were subjected to fast Fourier transform (FFT) to analyze their frequency characteristics. Each IMF component reflects the signal's characteristics within a specific frequency band. IMF 1–2 exhibit high-frequency components above 2000 Hz. IMF 3–5 represent middle- to high-frequency components ranging from 200 to 2000 Hz. IMF 6–11 are middle- to low-frequency components from 20 to 200 Hz. Finally, IMF 12–15 represents the low-frequency

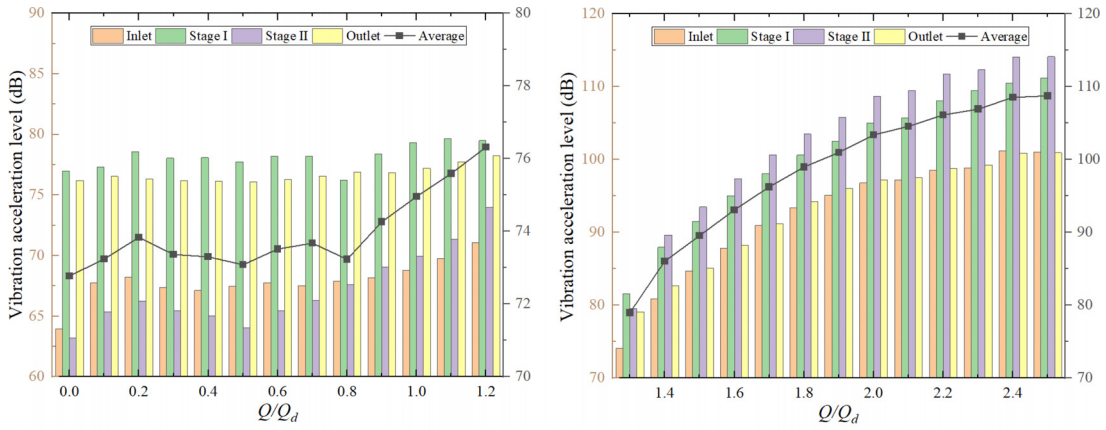

FIG. 20. VAL under different natural flow conditions.

components below 20 Hz. This decomposition allows for a more detailed analysis of the vibration signal within different frequency bands.

Figure 21 displays the differences in the characteristics of the vibration signal measured by the experiment at each frequency band as the flow rate increases. At $0.4Q_d$ working condition, because the impeller is stationary, it avoids the high-frequency vibration caused by the poor condition between the mechanical seal and bearing, and the imbalance of impellers or shaft swirl. Moreover, there is no rotor–stator interference between impeller and guide vane inside the pump, which reduces the vibration in the middle and high frequency band. Furthermore, the pump's stall vortex and backflow structure have large scales but relatively low energy, leading to slight vibration frequency fluctuation and amplitude.

When the flow rate increases to $1.0Q_d$, the impeller undergoes passive rotation, which may result in problems such as impeller imbalance, rotating shaft whirling, and poor mechanical seal operation. These factors can contribute to an increase in middle- to high-frequency vibrations. However, the low rotational speed makes the rise in vibration less intense. The effects of the rotor–stator interference and harmonics can be observed in IMF 10–11, which display the BPF and GVPF signals, respectively. The low-frequency band of IMF 12–15 mainly characterizes the stall vortex structure with high energy inside the pump.

Under the natural flow condition of $2.0Q_d$, the significant increase in both rotational speed and flow rate leads to sharp fluctuations in the high-frequency band, accompanied by noticeable increases in amplitude. The effects of the rotor–stator interference and harmonics are primarily concentrated between IMF 9–10. Moreover, the low-frequency vibration characteristics become more complex due to the influence of the more severe splitting and merging processes of the stall vortex inside the pump.

In order to further analyze the energy distribution characteristics of the vibration signal under natural flow conditions, a half-box plot analysis method was employed to examine the range, mean value, and localization of the vibration energy. Figure 22 presents the IMF-RMS energy distribution characteristics of the vibration signals at each measurement point for $0.4Q_d$, $1.0Q_d$, and $2.0Q_d$ natural flow conditions. At $0.4Q_d$, the impeller is in a stuck state, and its vibration energy primarily results from the impact of the natural flow. However, influenced by the flow loss, the average vibration energy decreases progressively stage by stage. The vibration level on the second stage of the pump is lower than the first stage by approximately 14.3%, and the interquartile range (IQR) of IMF-RMS is reduced.

When the flow rate is $1.0Q_d$, the liquid flow drives the impeller to passively rotate, resulting in increased vibration levels due to the rotor–stator interference. However, as the flow rate and rotational speed are relatively low, the vibration energy at the BPF is weak. In comparison with $0.4Q_d$, the vibration at the outlet experiences the largest increase, around 3.2 times. It can be attributed to the transfer of vibration energy from the pump body to the downstream region, as well as the turbulent pulsation effect caused by the outlet elbow structure. Moreover, the vibration increment on the inlet pipeline is primarily influenced by the natural flow impact boost, resulting in a rise of approximately 1.5 times. The vibration levels of both pump stages increase about 2.6 times, and the vibration level difference between the two stages decreases. The second stage is approximately 12.7% lower than the first stage, and the interquartile range of IMF-RMS increases.

At a flow rate of $2.0Q_d$, the rotational speed rises by 2.2 times relative to $1.0Q_d$. The overall vibration acceleration of the pump increases significantly, mainly due to the effects of the rotor–stator interference and the enhanced turbulent excitation force at high flow rates. The influence of turbulence intensity and stall vortex inside the pump increases stage by stage, making the vibration energy of the second stage about 1.5 times higher than that of the first stage. In contrast, the vibration level on the import and export pipeline is relatively close. In addition, during the rapid passive rotation of the impeller, potential problems such as imbalance of the impeller, swirl of the rotating shaft, and poor operation of the mechanical seal also lead to a rise in the intensity of medium- and high-frequency vibrations.

To investigate the effect of stall vortex and unsteady flow on the vibration time–frequency characteristics under natural flow conditions, the wavelet analysis is performed on the signals in the low- to middle-frequency bands after EMD decomposition. Figure 23 presents

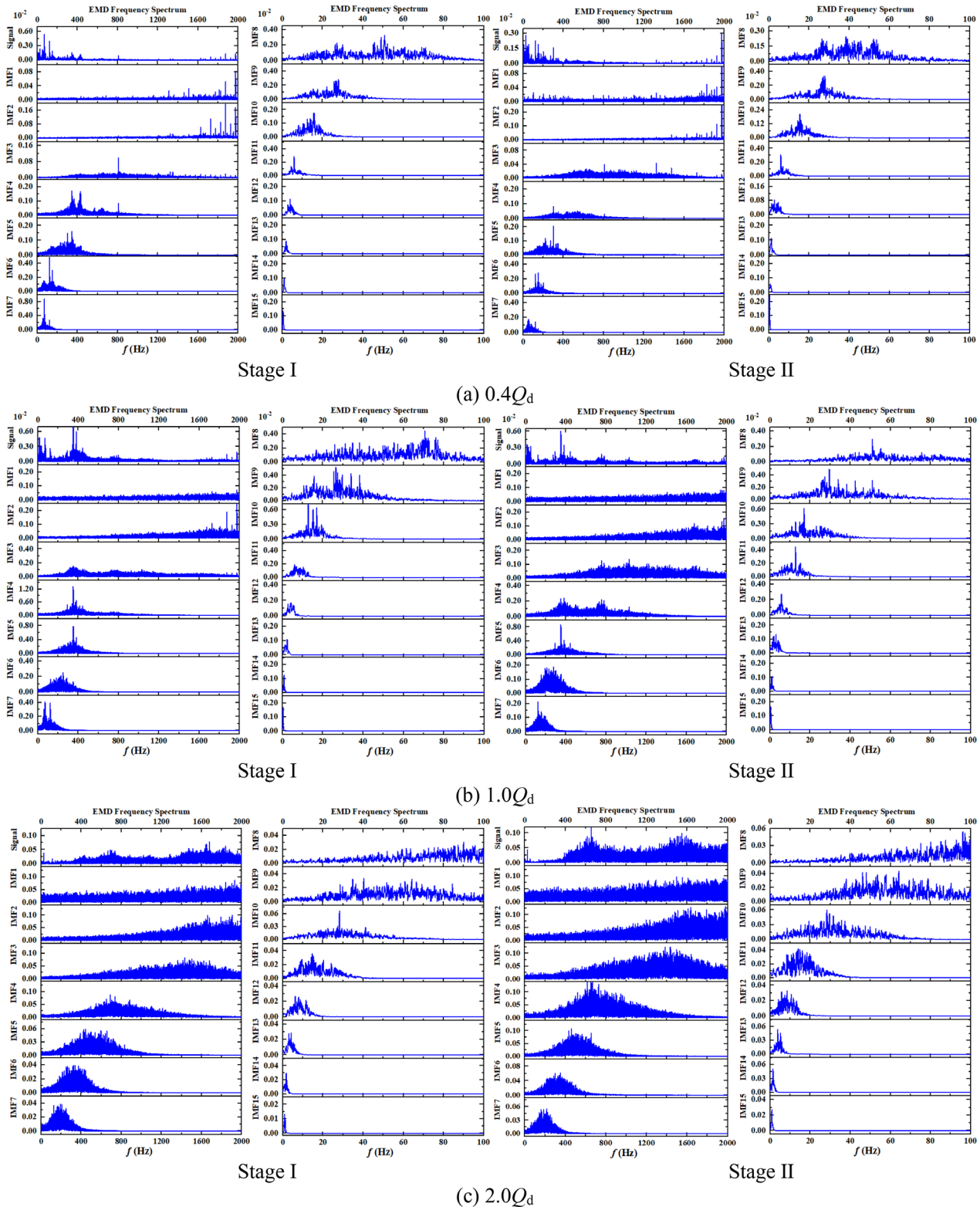

FIG. 21. EMD decomposition of vibration signal.

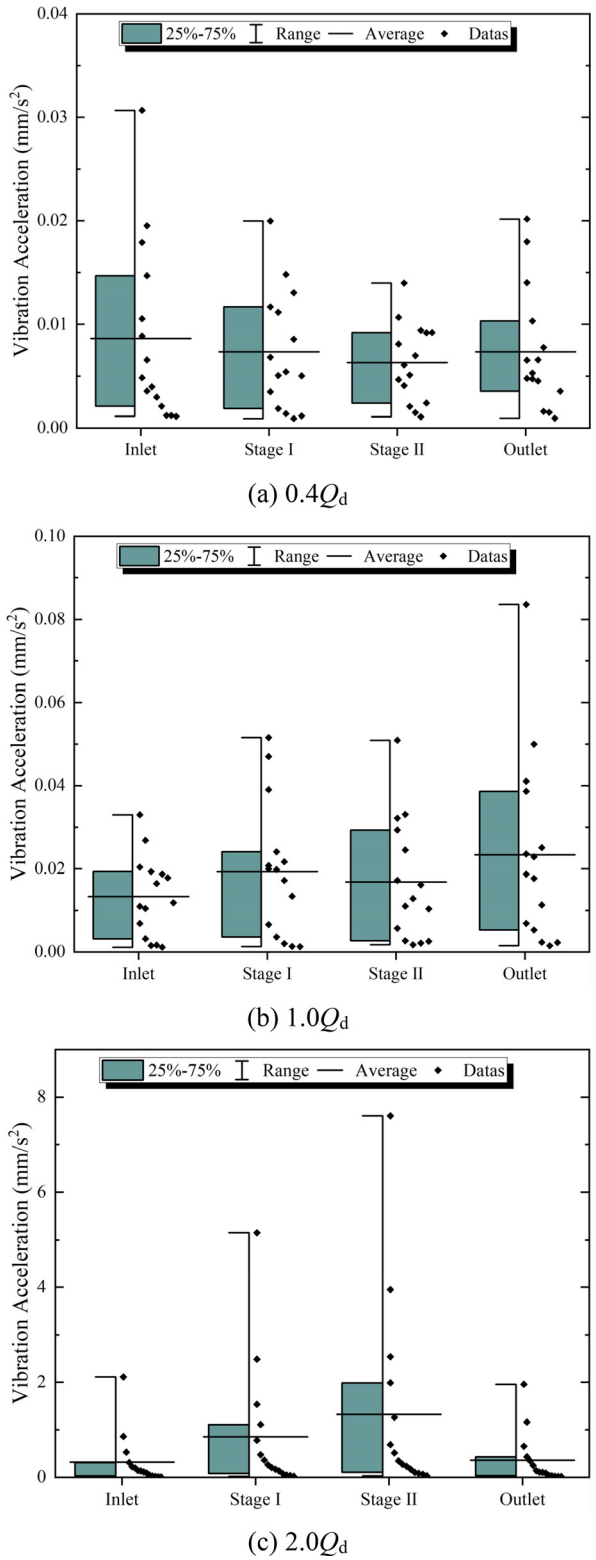

FIG. 22. IMF-RMS of the vibration under natural flow conditions.

the wavelet transform results of the vibration signal of the two-stage pump at different flow rates under natural flow condition. The energy of the vibration signal in the low- and middle-frequency bands is mainly concentrated within the 100 Hz frequency range. The average energy value increases with the rise in flow rate, and a significant peak modulus is observed in the time-averaged wavelet spectrum curve.

At a flow rate of $0.4Q_d$, the frequency range of the energy for the first stage is concentrated between 3 and 93 Hz, with the peak modulus at 42.5 Hz. It is wider than the 3–80 Hz range in the second stage, and the peak modulus frequency for the second stage pump is reduced to 35 Hz. When the flow rate increases to $1.0Q_d$, a portion of the kinetic energy is converted to mechanical energy required for the passive rotation of the impeller, and the overall vibration energy rises slightly. The time-averaged wavelet spectrum curve becomes steeper, and the energy frequency range narrows to 6–82 and 6–77 Hz for each pump stage. The peak modulus frequencies are 16 and 19 Hz, respectively. This is mainly due to the low-frequency disturbance caused by the internal stall vortex and the interference between the impeller and the guide vane.

At a high flow rate of $2.0Q_d$, significant differences are observed in the wavelet energy spectrum, with the vibration energy of the second-stage pump being more intense compared to the first stage. The wavelet energy in the low-frequency band increases, and the spectrum range extends to higher frequencies. The range of each stage is 0–101 and 0–115 Hz, and the peak modulus frequencies are 14 and 20 Hz, respectively. The time-averaged wavelet spectral curve is smoother compared to the lower flow rates.

IV. CONCLUSIONS

This research investigated the correlation between stall vortex and vibration characteristics of a two-stage pump under natural flow conditions based on numerical simulations and vibration experiments. The *Q*-criterion and vorticity transport equation were employed to examine the structure and motion characteristics of the stall vortex under different natural flow conditions. Furthermore, the vibration signals were processed and analyzed by combining singular value decomposition, empirical modal decomposition, and wavelet analysis methods. The main conclusions are as follows:

(1) Under natural flow conditions, the impeller's motion state can be categorized into two modes: stuck and passively rotating. Due to the inlet flow angle not matching the blade angle, a large region of stall vortex is formed near the blade's pressure side. The rotational speed increases linearly with the flow rate during passive rotation, resulting in a relatively invariant inlet attack angle at different flow rates, making the internal flow features similar. The stretching and bending of the stall vortex structure primarily cause the variation of the vorticity. The effect of Coriolis forces caused by passive rotation is closely correlated to the stall vortex structure inside the impeller. Moreover, the viscous force inhibits the vortex evolution, but its viscous dissipation effect is relatively weak.

(2) The excitation force of each stage increases continuously with the natural flow rate. At low flow rates, the excitation force is affected equally by the wall static pressure and the turbulent kinetic-induced dynamic pressure. While as the flow rate increases, the influence of static pressure on the excitation force plays a dominant role. The main frequency inside the impeller

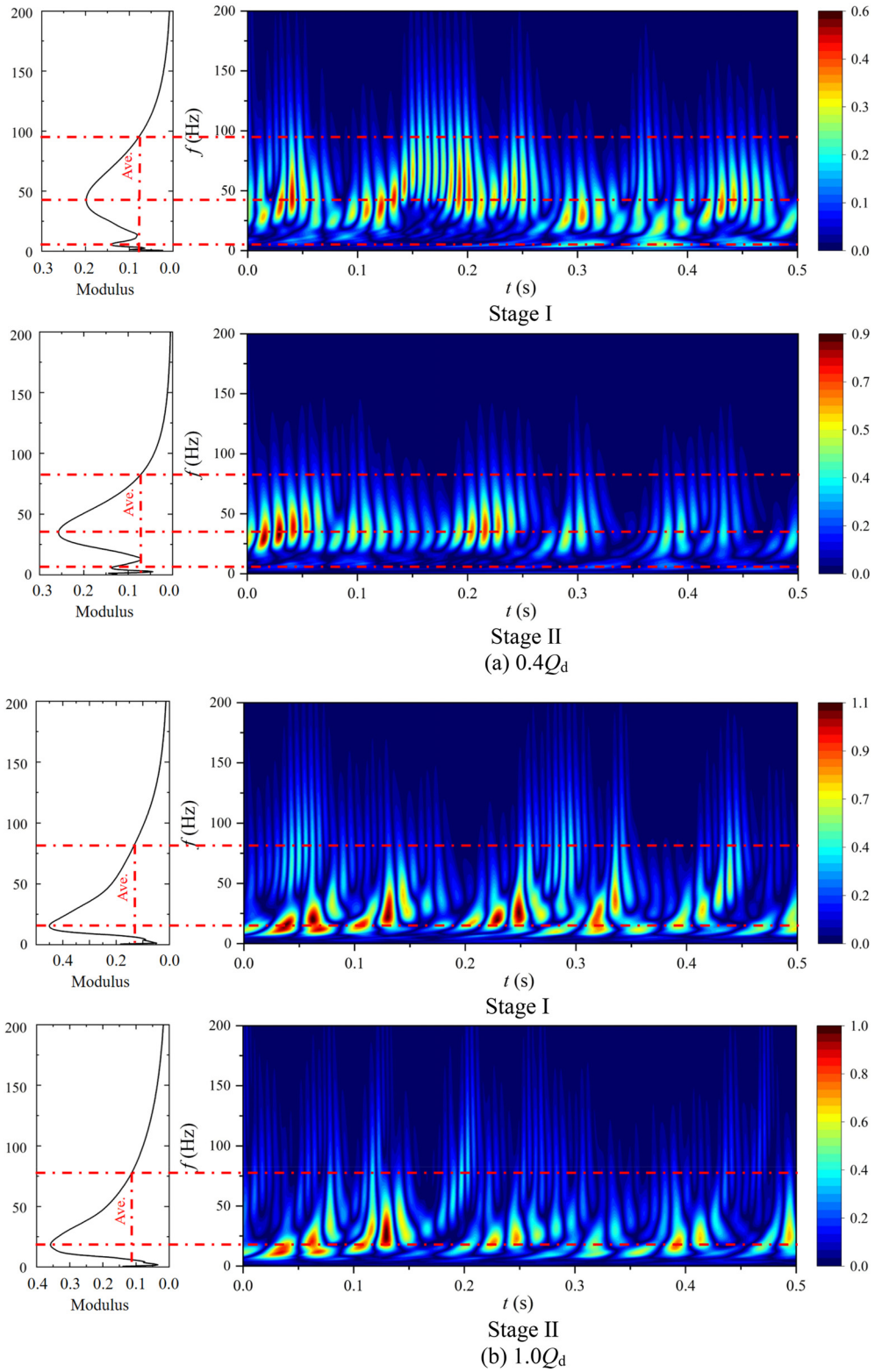

FIG. 23. Wavelet mode spectrum of vibration signals under different natural flow conditions.

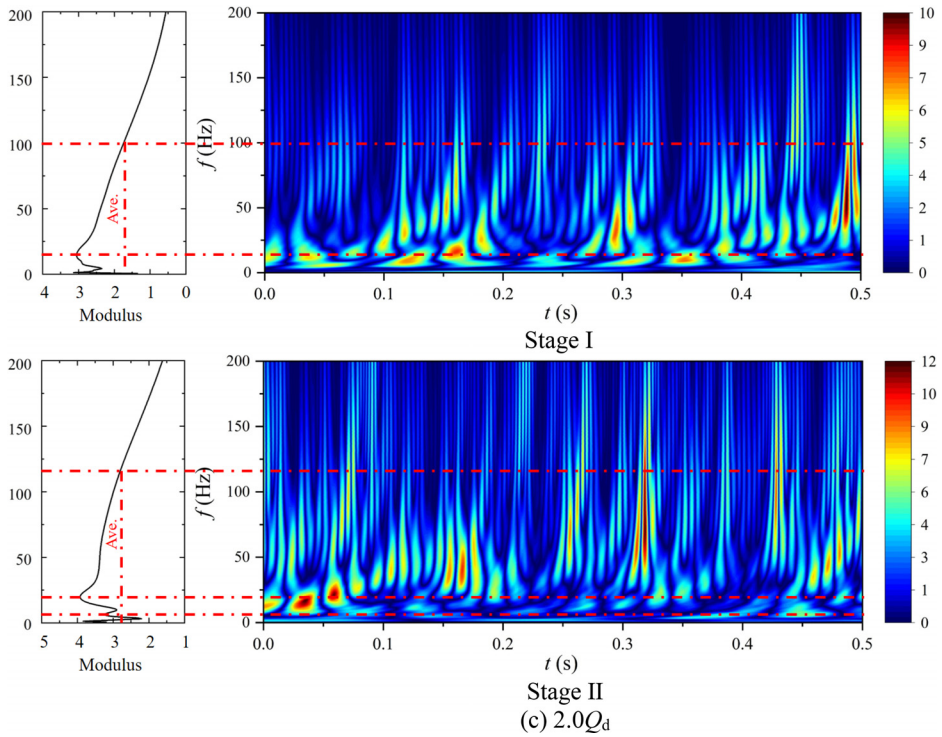

FIG. 23. (*Continued.*)

is at the GVPF, and the secondary frequency is twice GVPF. Furthermore, the main frequency inside the guide vane is BPF. The main frequency of the total radial excitation force is primarily distributed at the quadruple BPF (triple GVPF), which is the harmonic frequency between BPF and GVPF.

(3) At a flow rate of $0.4Q_d$, the impeller remains in a stuck condition, leading to the formation of a large-scale stall vortex structure inside the pump. The vibration energy is mainly concentrated in the low-frequency band and decreases stage by stage. As the flow rate rises to $1.0Q_d$, the impeller transitions into passive rotation, giving rise to certain issues such as rotating shaft whirling and poor mechanical seal operation. It leads to an increase in the middle- to high-frequency vibration. However, this increase is moderate due to the relatively low rotational speed. At a high flow rate of $2.0Q_d$, the turbulence level and the impact of the stall vortex inside the second-stage pump gradually increase stage by stage, resulting in significantly higher vibration energy in the second stage compared to the first stage. The vibration signal exhibits sharp fluctuations in the high-frequency band, with a significant increasing amplitude.

(4) The vibration energy caused by the stall vortex is in the middle- to low-frequency band below 100 Hz. The average vibration energy increases with the rise of flow rate, and the time-averaged wavelet spectrum curve exhibits a distinct peak modulus. The low-frequency disturbance caused by the stall vortex and the rotor–stator interference is the main reason for the intense variation of the wavelet energy with time. At a flow rate of 0.4 Q_d, the vibration energy of the first-stage pump is concentrated within the frequency band of 3–93 Hz, with the peak modulus at 42.5 Hz. The peak modulus frequency of the second-stage pump is 35 Hz. When the flow rate increases to 1.0 Q_d, the vibration energy experiences a slight increment. However, the time-averaged wavelet spectral curve becomes steeper, and the peak modulus frequency decreases to 16 and 19 Hz. At a flow rate of $2.0Q_d$, the wavelet energy in the low-frequency band increases, expanding the spectral range toward high-frequency. Additionally, the time-averaged wavelet spectral curve is flatter than the low flow rate.

ACKNOWLEDGMENTS

The authors would like to thank the financial support from the National Natural Science Foundation of China (Nos. 52279087 and 51879122), Zhenjiang key research and development plan (Nos. GY2017001 and GY2018025), the Open Research Subject of Key Laboratory of Fluid and Power Machinery, Ministry of Education, Xi-hua University (Nos. szjj2017094 and szjj2016068), Sichuan Provincial Key Lab of Process Equipment and Control (Nos. GK201614 and GK201816), Jiangsu University Young Talent training Program-Outstanding Young backbone Teacher, Program Development of Jiangsu Higher Education Institutions (PAPD), and Jiangsu top six talent summit project (No. GDZB-017).

AUTHOR DECLARATIONS

Conflict of Interest

The authors have no conflicts to disclose.

Author Contributions

Runze Zhou: Conceptualization (equal); Data curation (equal); Methodology (equal); Software (equal); Writing – original draft (equal). **Houlin Liu:** Conceptualization (equal); Funding acquisition (equal); Project administration (equal); Resources (equal). **Liang Dong:** Project administration (equal); Resources (equal); Supervision (equal). **Kim Tiow Ooi:** Supervision (lead); Writing – review & editing (equal). **Cui Dai:** Project administration (equal); Supervision (equal). **Ru Nan Hua:** Project administration (equal); Resources (equal).

DATA AVAILABILITY

The data that support the findings of this study are available from the corresponding author upon reasonable request.

REFERENCES

[1]Y. Liu and L. Tan, "Tip clearance on pressure fluctuation intensity and vortex characteristic of a mixed flow pump as turbine at pump mode," Renewable Energy **129**, 606–615 (2018).

[2]W. Li, L. Ji, W. Shi *et al.*, "Vibration of shaft system in the mixed-flow pump induced by the rotor-stator interaction under partial load conditions," Shock Vib. **2018**, 2059784.

[3]M. Sinha, A. Pinarbasi, and J. Katz, "The flow structure during onset and developed states of rotating stall within a vaned diffuser of a centrifugal pump," J. Fluids Eng. **123**(3), 490–499 (2001).

[4]X. D. Liu, Y. J. Li, Z. Q. Liu *et al.*, "Dynamic evolution process of rotating stall vortex based on high-frequency PIV system in centrifugal impeller," Ocean Eng. **259**, 111944 (2022).

[5]J. Feng, Z. Ge, H. Yang *et al.*, "Rotating stall characteristics in the vaned diffuser of a centrifugal pump," Ocean Eng. **229**, 108955 (2021).

[6]P. Zhou, J. Dai, Y. Li *et al.*, "Unsteady flow structures in centrifugal pump under two types of stall conditions," J. Hydrodyn. **30**(6), 1038–1044 (2018).

[7]W. Li, L. Ji, E. Li *et al.*, "Numerical investigation of energy loss mechanism of mixed-flow pump under stall condition," Renewable Energy **167**, 740–760 (2021).

[8]W. Li, E. Li, L. Ji *et al.*, "Mechanism and propagation characteristics of rotating stall in a mixed-flow pump," Renewable Energy **153**, 74–92 (2020).

[9]L. Ji, W. Li, W. Shi *et al.*, "Diagnosis of internal energy characteristics of mixed-flow pump within stall region based on entropy production analysis model," Int. Commun. Heat Mass Transfer **117**, 104784 (2020).

[10]Z. Zhao, W. Song, Y. Jin *et al.*, "Numerical study on flow stall and kinetic energy conversion of low-specific-speed centrifugal pump," Phys. Fluids **35**(4), 044104 (2023).

[11]X. Q. Jia, H. Lv, and Z. C. Zhu, "Research on the influence of impeller tip clearance on the internal flow loss of axial circulating pump under unpowered driven condition," J. Fluids Eng. **145**(2), 021202 (2023).

[12]X. Q. Jia, H. Lv, K. Rao *et al.*, "Research on pressure fluctuation induced by tip leakage vortex of axial flow circulating pump under unpowered driven conditions," Phys. Fluids **35**(3), 034118 (2023).

[13]X. Jia, H. Lv, S. Zhang *et al.*, "Research on tip leakage vortex characteristics of axial-flow circulating pumps under unpowered driven conditions," Proc. Inst. Mech. Eng., Part E: J. Process Mech. Eng. (published online 2023).

[14]X. Luo, J. Yang, and L. Song, "Analysis and research on vibration characteristics of nuclear centrifugal pumps at low flow rates," Energy Rep. **8**, 1273–1282 (2022).

[15]L. Bai, L. Zhou, X. Jiang *et al.*, "Vibration in a multistage centrifugal pump under varied conditions," Shock Vib. **2019**, 2057031.

[16]A. E. Khalifa, A. M. Al-Qutub, and R. Ben-Mansour, "Study of pressure fluctuations and induced vibration at blade-passing frequencies of a double volute pump," Arabian J. Sci. Eng. **36**, 1333–1345 (2011).

[17]C. Wang, X. Chen, N. Qiu *et al.*, "Numerical and experimental study on the pressure fluctuation, vibration, and noise of multistage pump with radial diffuser," J. Braz. Soc. Mech. Sci. Eng. **40**, 1–15 (2018).

[18]K. Pu, B. Huang, H. Miao *et al.*, "Quantitative analysis of energy loss and vibration performance in a circulating axial pump," Energy **243**, 122753 (2022).

[19]B. Cui, Y. Zhang, and Y. Huang, "Analysis of the pressure pulsation and vibration in a low-specific-speed centrifugal pump," J. Fluids Eng. **143**(2), 021201 (2021).

[20]L. Wang, J. Lu, W. Liao *et al.*, "Numerical investigation on vibration and pressure fluctuation characteristics in a centrifugal pump under low flow rate," Proc. Inst. Mech. Eng., Part C: J. Mech. Eng. Sci. **235**(19), 3888–3899 (2021).

[21]J. Lu, Y. Gong, L. Li *et al.*, "Research of the vibration induced by cavitation in a centrifugal pump under part load condition," Phys. Fluids **35**(4), 045144 (2023).

[22]S. Dong, J. Duan, and T. Sun, "Dynamic response and acoustic characteristics of composite hydrofoil under cavitation-induced vibration," Phys. Fluids **35**(1), 013302 (2023).

[23]A. R. Al-Obaidi and H. Towsyfyan, "An experimental study on vibration signatures for detecting incipient cavitation in centrifugal pumps based on envelope spectrum analysis," J. Appl. Fluid Mech. **12**(6), 2057–2067 (2019).

[24]A. R. Al-Obaidi, "Investigation of effect of pump rotational speed on performance and detection of cavitation within a centrifugal pump using vibration analysis," Heliyon **5**(6), e01910 (2019).

[25]R. Zhou, H. Chen, L. Dong *et al.*, "Effect of vibration and noise measuring points distribution on the sensitivity of pump cavitation diagnosis," Strojniški Vestn.-J. Mech. Eng. **68**(5), 325–338 (2022).

[26]Y. Luo, W. Zhang, Y. Fan *et al.*, "Analysis of vibration characteristics of centrifugal pump mechanical seal under wear and damage degree," Shock Vib. **2021**, 6670741.